A Generalized Input Impedance Model of Multiple Active Bridge Converter

Jiajun Yang, *Student Member, IEEE*, Giampaolo Buticchi, *Senior Member, IEEE*, Chunyang Gu, *Member, IEEE*, Sandro Günter, *Member, IEEE*, He Zhang, *Member, IEEE*, and Pat Wheeler, *Senior Member, IEEE*

***Abstract*—The electrical power distribution system (EPDS) of the more electric aircraft (MEA) is a fundamental component that needs to be efficient and resilient. The commonly considered architectures feature separate buses to achieve separation between different sub-sections of the EPDS. Although effective, this implies an over design, since all sub-sections are sized for the local worst-case scenarios. In the MEA concept, multi-port converters could connect the whole EPDS while guaranteeing the galvanic isolation between buses. Since multi-port converters would give rise to a completely different EPDS topology, dominated by power electronics interfaces, the stability of such a system must be assessed. This paper investigates the input impedance of multiple active bridge (MAB) converters when interfaced to a single DC bus and multiple resistive loads. A transfer function based input impedance model of the MAB converter is proposed. To validate the proposed input impedance model, the verification of input impedances of a triple active bridge (TAB) converter and a quadruple active bridge (QAB) converter are carried out using both simulation and experimental results.**

***Index Terms*— DC microgrid, input impedance, multi-port DC-DC converter, more electric aircraft.**

I. Introduction

Nowadays, the concept of the more electric aircraft (MEA) has attracted more and more consideration by researchers, which is aimed at electrifying the subsystems on aircraft. In recent years, several projects have been started to achieve the electrification of subsystems on aircraft, such as Totally Integrated More Electric Systems (TIMES) sponsored by the Department of Trade and Industry (DTI) under the Civil Aircraft Research And technology Demonstration (CARAD) programme [1] and More Electric Initiative developed by the US Air Force Research Laboratory [2]. In a MEA, most of onboard pneumatic, hydraulic and mechanical devices are supposed to be replaced by electrical devices, benefiting the aircraft with lower weight, lower maintenance cost and lower environmental impact [3]. So far, significant progress has been made in the electrification of subsystems on aircraft, for example, the main engine generator is directly coupled to the jet engine via a gearbox without the integrated drive generator (IDG) in the latest and the most advanced commercial aircraft, including the Boeing 787 and the Airbus A380 [4].

As on-board electrical devices increase, the demands of electrical power increase, resulting in an on-board electrical power systems (EPS) with larger size and heavier weight. Meanwhile, the architecture and individual subsystems of the EPS become more complicated, increasing the potential risks of instability. Besides, the large-scale redundancy of electrical power distribution system (EPDS) is supposed to be minimized to diminish the overall installed power in an aircraft, which increases the unpredictability of power requested [5]. To meet the different requirements of power according to the number of installed power electronic converters and the characteristics of actuators, a number of voltage standards including both AC and DC levels on commercial aircraft exist [6]. Since the aircraft can be regarded as an isolated system with generators and loads, the EPDS can be regarded as an onboard microgrid [7]. Compared to the AC microgrid, the DC microgrid has attracted interest from researchers due to the advantages of fewer conversion stages and lower current ratings, simplifying the architecture and improving the efficiency [8]. Fig. 1 shows a simplified structure of DC microgrid for a MEA. It can be observed that the DC microgrid may contain several AC-DC converters to convert AC waveforms from generator to DC and many DC-DC converters to achieve different DC voltage levels for the various loads. Whereas the DC microgrid contains many individual converters and communication devices among converters due to the multiple conversion stages and load characteristic, the structure is still complex and the cost is high. To cope with these challenges, the concept of multi-port DC-DC converters was proposed in [9], to reduce the number of conversion stages by combining individual DC-DC converters

This work was supported in part by the Natural Science Foundation of Zhejiang Province under Grant LQ19E070002, and in part by the Ningbo Municipal Bureau of Science and Technology under Grant 2018A610146 and Grant 2018B10082. *(Corresponding author: Chunyang Gu.)*

Jiajun Yang, Giampaolo Buticchi, Chunyang Gu and He Zhang are with the Key Laboratory of More Electric Aircraft Technology of Zhejiang Province, University of Nottingham Ningbo China, Ningbo, China (e-mail: jiajun_yang@outlook.com; giampaolo.buticchi@nottingham.edu.cn; chunyang.gu@nottingham.edu.cn; he.zhang@nottingham.edu.cn).

Sandro Günter is with the E3/DC GmbH, Karlstraße 5, D-49074 Osnabrück, Germany. (e-mail: sandro.guenter@e3dc.com).

Pat Wheeler is with the Key Laboratory of More Electric Aircraft Technology of Zhejiang Province, University of Nottingham Ningbo China, Ningbo, China and the University of Nottingham, Nottingham NG7 2RD, U.K. (e-mail: pat.wheeler@nottingham.edu.cn).

in an integrated converter with multiple inputs and outputs.

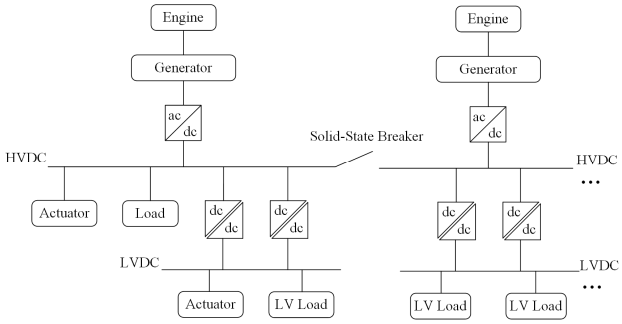

Fig. 1. The basic structure of DC microgrid on MEA

Considering the safety requirement of the MEA, the installed DC-DC power converters must have galvanic isolation [5], [7]. Among a variety of DC-DC converters, the dual active bridge (DAB) converter is one of the most popular topology because of its bidirectional power flow, high efficiency, high power density, low device and component stresses and low switching losses [10]. Benefiting from the DAB converter, it becomes a consensus to most researchers that it is better if the feature of multi-port DC-DC converters can imitate the DAB converter, i.e. multiple active bridge (MAB) converters which contain multiple H-bridges and a multi-winding high frequency (HF) transformer. Some researches about multi-port DC-DC converters has been published, including investigations of the triple active bridge (TAB) converter and the quadruple active bridge (QAB) converter [11], [12].

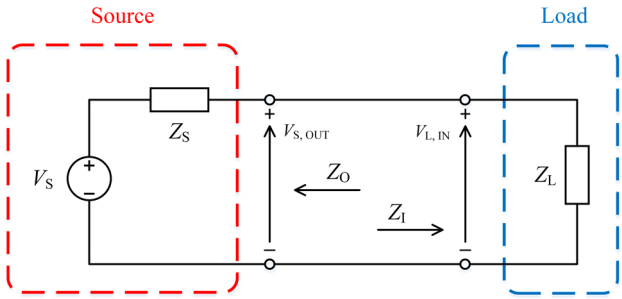

Fig. 2. The equivalent circuit of a DC system

Although multi-port DC-DC converters are expected to replace the single-input-single-output (SISO) DC-DC converters in microgrids, the effects of them on system stability needs to be assessed. There are several methods to analyze stability. Among these methods, the impedance-based method is preferred by the majority of researchers because the system stability can be readily evaluated by modeling the impedance of system. Changes of the system structure and the parameters of sources or loads only influence the impedance characteristics [13]. Fig. 2 shows the equivalent circuit of a DC system consisting of two individual stable subsystems. To assess the stability of DC systems based on impedance, the concept of minor loop gain (MLG) is introduced, which is the ratio of the output impedance Z_O of source subsystem and the input impedance Z_I of load subsystem. The MLG is also the term responsible for stability in the input-to-output transfer function of the whole system [14]. Using the Nyquist Criterion, the system will be stable if the minor loop gain does not encircle (-1, 0) in Nyquist contour. Based on this, several stability criteria have been proposed, the most conservative is the Middlebrook Criterion [15]. The stability condition of the Middlebrook Criterion can be expressed as

$$\left|\frac{Z_O}{Z_I}\right| < \frac{1}{GM} \quad (GM > 1) \tag{1.1}$$

where GM is the expected gain margin. Although the Middlebrook Criterion can ensure the stability of a system, it could sacrifice the size of system by implementing large passive components in the input filter design [14], [16]. To avoid this overdesign, the Gain Margin Phase Margin (GMPM) Criterion was proposed in [17], which is more moderate by giving conditions in both gain margin and phase margin to system design. The stability condition of GMPM Criterion can be given as

$$\left|\frac{Z_O}{Z_I}\right| < \frac{1}{GM}, \text{ if not, } |\angle Z_O - \angle Z_I| \le 180° - PM \tag{1.2}$$

where GM is the expected gain margin and PM is the expected phase margin. It is obvious that the GMPM Criterion gives a less restrictive condition by considering the phase margin when the gain condition is not satisfied. However, the GMPM Criterion requires the information of the amplitude and phase of subsystems, and proper design for gain margin and phase margin [14]. So far, some works related to the impedance-based stability analysis of systems have been done. It is shown in [18] that the stability issues caused by DC-link voltage control of grid-connected voltage-source converters can be investigated and addressed by analyzing the impedance of the grid and the converter. It is also shown in [19] that the stability of a single DC-bus, multi-generator EPS supplying a constant power load (CPL) can be analyzed in terms of the impedance of the source and load subsystems, with the cases of different number of generators and power sharing ratio. Therefore, it is credible that the impedance-based method can be used to assess the stability of large systems by modeling the impedance of subsystems inside.

As the DC-DC converters are supposed to connect to the DC buses in EPDS, to avoid the instability issues, it is necessary to find the input impedance and output impedance of DC-DC converters. In this paper, a generalized input impedance model of MAB converter is proposed and validated with both simulation and experimental results. Section II presents the power transmission characteristics of a MAB converter. Section III gives the deduction of generalized input impedance model of MAB converter based on power equations of any two ports. Section IV provides the reasonable specifications for a MAB converter applied for MEA. Section V validates the generalized input impedance model in terms of simulating the switching model of TAB converter and QAB converter. Section VI shows the experimental results. Section VII summarizes the work and draw the conclusions.

II. Multiple Active Bridge Converter

In general, the MAB converters can be interfaced with buses and a variety of loads to achieve the simultaneous power flow between any two ports. In this paper, the MAB converter is supposed to connect to a single bus and several resistive loads, and the generalized input impedance model of it is investigated and derived.

Fig. 3 shows the basic structure of MAB converters. Port 1 is

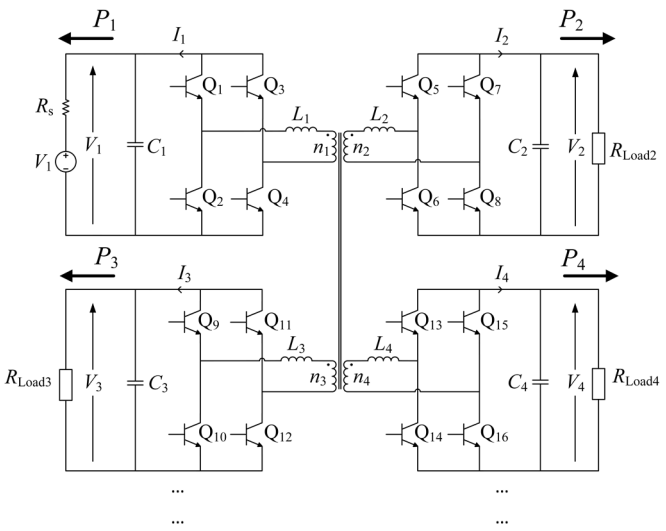

Fig. 3. The basic structure of MAB converters

connected to DC bus while the other ports are connected to different resistive loads. By enabling the single phase shift modulation of all H-bridges, the multidirectional power flow among all ports can be achieved. Assuming that the MAB converter has n ports in total, the individual power transmitted between any two ports can be given as

$$P_{m,j} = \frac{V_m V_j}{2N_{m,j} f_S L_{m,j}} d_{m,j}\left(1 - \left|d_{m,j}\right|\right) \quad (m, j = 1, 2, \dots, n \text{ and } m \neq j) \tag{2.1}$$

where V_m and V_j are the port voltage of Port m and Port j, $N_{m,j}$ are the turn ratio between Port m and Port j, $L_{m,j}$ is the leakage inductance between Port m and Port j, $d_{m,j}$ is the phase shift ratio normalized to π.

Consider the conservation of power, the total power in Fig. 3 satisfy the equation

$$P_1 + P_2 + P_3 + \cdots + P_n = 0 \ \ (n \geq 2, n \in N^*) \tag{2.2}$$

Since the power of each port can be regarded as the combination of individual power between any two ports. The equation of power of port j can be written as

$$P_j = \sum_{m=1, m\neq j}^{n} P_{j,m} \quad (j = 1, 2, \dots, n) \tag{2.3}$$

To obtain the real leakage inductance in (2.1), the appropriate transformer model needs to be worked out. Fig. 4 shows different kinds of transformer models, containing both star model and delta model. In Fig. 4(b) which is the star model, the leakage inductance and the voltage of each port referring to Port 1 are calculated as

$$L_j' = \left(\frac{N_1}{N_j}\right)^2 L_j \quad (j = 1, 2, \dots, n) \tag{2.4}$$

$$V_j' = \frac{N_1}{N_j} V_j \quad (j = 1, 2, \dots, n) \tag{2.5}$$

Since the star model can only represent the leakage inductance and the voltage of each port referring to the specific port, it cannot be used to obtain the leakage inductance of MAB converter in which the leakage inductance is coupled. To model the leakage inductance of MAB converter properly, the delta model is adopted. The methodology of delta model for a triple active bridge (TAB) converter was introduced in [20]. Based on that and assuming the magnetizing inductance is so large that it can be regarded as an open circuit, the inductance between each two ports of MAB converter can be deduced as

$$L_{m,j} = \frac{\sum_{k=1}^{n}\left(\prod_{a=1, a\neq k}^{n} L_a'\right)}{\prod_{i=1, i\neq m, i\neq j}^{n} L_i'} \quad (m, j = 1, 2, \dots, n \text{ and } m \neq j) \tag{2.6}$$

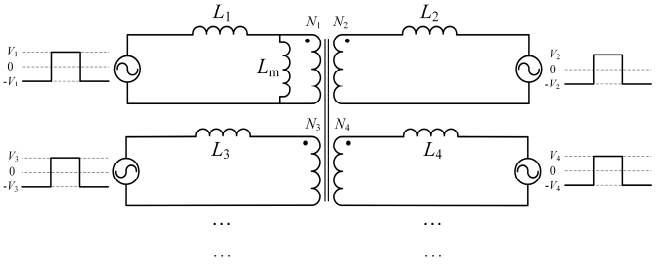

(a) Original transformer model of MAB converters

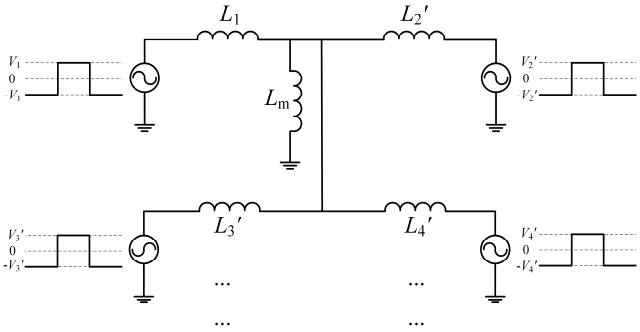

(b) Star model of MAB converters

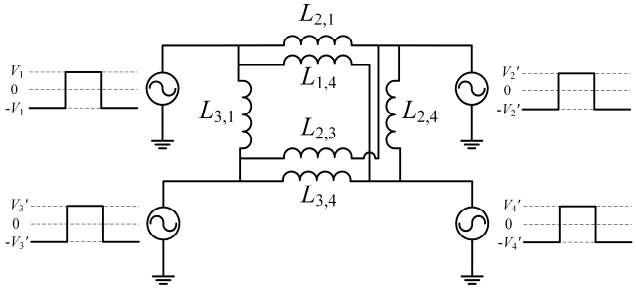

(c) Delta model of QAB converter for example

Fig. 4. The transformer models of MAB converters

III. Generalized Small Signal Model of MAB Converter

State-space averaging and circuit averaging are two conventional techniques to obtain the small signal model of converters [21]. Both techniques can show the system dynamics and the coupling among system state variables. The state-space averaging technique allows to derive the small signal model with the known system state equations, while the circuit averaging technique allows to manipulate on the circuit diagram directly if the waveforms of switch terminal over a switching period are known. However, both two techniques need detailed information of the system to achieve high accuracy of modeling. When it comes to the converter with

more components, it becomes difficult to obtain the small signal model by using these two techniques. An input impedance model of DAB converter based on improved state-space averaging technique was proposed in [22], where the AC components are also considered for state variables and the computation procedure is complex. By contrast, a transfer function block scheme based on the small signal equations derived from power equation of DAB converter was proposed in [23], which is apparently much easier. Based on that, an input impedance model of TAB converter has been worked out in [24]. In this section, a further generalized model of the input impedance of MAB converter is developed. According to (2.1) and (2.3), the average current of port j can be written as

$$I_j = \sum_{m=1,m\neq j}^{n} \frac{V_m}{2N_{j,m}f_s L_{j,m}} d_{j,m}\left(1-\left|d_{j,m}\right|\right) \ (j=1,2,\dots,n) \tag{3.1}$$

The small signal equation of port current is worked out by deriving (3.1) partially to voltages and phase shift ratios which is represented in (3.2) in the next page. Note that the $d_{j,m}$ is substituted by $d_{j,1}$-$d_{m,1}$, since this substitution will simplify the structure of the transfer function block scheme by using fewer phase shift ratios. To get the input impedance of MAB converter in a more organized way, the gains are numerically sorted and labelled. Based on (3.2), there are totally $2n^2$-$2n$ small signal gains and they are defined in Table I in the next page, where T_D is a first order delay function with time constant of one switching period.

Fig. 5 in the next page shows the transfer function block scheme. It can be seen that the small signals on each branch also have effects on other branches, and this coupling between branches makes the derivation of input impedance more difficult. Hence, it is necessary to perform decoupling technique to separate each branch. The small signals in Table I can be represented as

$$\begin{cases} \hat{d}_{j,1} = \frac{G_{\text{Branch},j}}{G_{2j-2}} & (j=2,3,\dots,n) \\ \hat{V}_m = \frac{G_{\text{Branch},m}}{-G_{2m-2}G_{\text{Ctrl},m}} & (m=2,3,\dots,n) \\ \hat{d}_{m,1} = \frac{G_{\text{Branch},m}}{G_{2m-2}} & (m=2,3,\dots,n) \end{cases} \tag{3.3}$$

where $G_{\text{Branch},j}$ and $G_{\text{Branch},m}$ are the final gains of "Branch j" and "Branch m" shown in Fig. 5, $G_{\text{Ctrl},m}$ and $G_{\text{Ctrl},j}$ are the transfer function of "Controller m" and "Controller j", $G_{\text{Load},j}$ is the transfer function of "Load j", $G_{2j\text{-}2}$ and $G_{2m\text{-}2}$ are the numerically labelled small signal gains in Table I. Combining Table I and (3.3) with the block scheme, the equation of all branches to $\hat{V}_1$ yields

$$\begin{aligned} \hat{V}_1 &= \frac{G_{(j-1)(2n-2)+2}G_{\text{Ctrl},j}G_{\text{Load},j}+1}{-G_{2j-2}G_{Ctrl,j}G_{\text{Load},j}G_{(j-1)(2n-2)+1}}G_{\text{Branch},j} \\ &+ \sum_{m=2}^{j-1}\frac{\left(G_{\text{Ctrl},m}G_{2m+(j-1)(2n-2)}-G_{2m+(j-1)(2n-2)-1}\right)}{-G_{2m-2}G_{\text{Ctrl},m}G_{(j-1)(2n-2)+1}}G_{\text{Branch},m} \\ &+ \sum_{m=j+1}^{n}\frac{\left(G_{\text{Ctrl},m}G_{2m+(j-1)(2n-2)-2}-G_{2m+(j-1)(2n-2)-3}\right)}{-G_{2m-2}G_{\text{Ctrl},m}G_{(j-1)(2n-2)+1}}G_{\text{Branch},m} \\ &\qquad (j=2,3,\dots,n) \end{aligned} \tag{3.4}$$

As (3.4) shows, $\hat{V}_1$ is influenced by each branch. This can be re-arranged to be a matrix shown in (3.5) in the next page. Since it is aforementioned that the branches are also coupled together, to cancel the coupling effects, (3.5) is transformed as

$$\{\boldsymbol{B}\} = \boldsymbol{A}^{-1}\{\hat{V}_1\} \tag{3.6}$$

where $\boldsymbol{B}$ is the matrix of branches and $\boldsymbol{A}^{-1}$ is the inverse of Matrix $\boldsymbol{A}$. By performing this transformation, the branches are decoupled and can be represented by $\hat{V}_1$ only. By summing the elements in each row of $\boldsymbol{A}^{-1}$, the coefficients vector of $\hat{V}_1$ can be obtained. Thus, (3.6) can be written as

$$\begin{Bmatrix} G_{\text{Branch},2} \\ G_{\text{Branch},3} \\ \vdots \\ \vdots \\ G_{\text{Branch},n} \end{Bmatrix} = \begin{Bmatrix} Coef_2 \\ Coef_3 \\ \vdots \\ \vdots \\ Coef_n \end{Bmatrix}\{\hat{V}_1\} \tag{3.7}$$

Combining Table I, (3.3) and (3.7), the equation of $\hat{I}_1$ can be obtained as

$$\hat{I}_1 = \sum_{m=2}^{n}\left(1+\frac{G_{2m-3}}{-G_{2m-2}G_{\text{Ctrl},m}}\right)Coef_m\hat{V}_1 \tag{3.8}$$

Considering the direction of current I_1 and input capacitor C_1 in Fig. 3, the input impedance of MAB converter is calculated as

$$Z_{\text{in,MAB}} = \frac{1}{-\sum_{m=2}^{n}\left(1+\frac{G_{2m-3}}{-G_{2m-2}G_{\text{Ctrl},m}}\right)Coef_m+sC_1} \tag{3.9}$$

IV. Specifications of MAB Converter in MEA

With the structure of MAB converter shown in Fig. 3, to facilitate the calculation and observation of power flow inside the MAB converter, all H-bridges are designed to be same, leading to a symmetrical structure of the converter. Considering the requirements and standards of MEA, a set of feasible parameters for simulation are listed in Table II.

TABLE II
Simulation Parameters

Symbol	Definition	Value
V_1, V_2…V_n	Port voltage	270 V
C_1, C_2…C_n	Capacitor	0.34 mF
L_1, L_2…L_n	Leakage inductance	20 uH
f_s	Switching frequency	50 kHz
N_1:N_2:…:N_n	Turn ratio of transformer	1:1:…:1
K_{p2}, K_{p3}…K_{pn}	Proportional coefficient	0.1
K_{i2}, K_{i3}…K_{in}	Integral coefficient	10
$d_{2,1}$, $d_{3,1}$…$d_{n,1}$	Phase shift ratio	-0.2 → 0.2
R_{Load2}, R_{Load3}…$R_{\text{Load}n}$	Resistance of load	$\frac{25nf_sL}{2}$ ohm → ∞
R_s	Source resistance	0.1 ohm

Since the converter will be unstable if the phase shift ratio goes out of the nearly linear operating region (-0.5, 0.5), the phase shift ratios $d_{2,1}$, $d_{3,1}$…$d_{n,1}$ are limited in (-0.2, 0.2). This limitation indirectly ensures the potential phase shift ratios such as $d_{2,3}$, which is the difference of $d_{2,1}$ and $d_{3,1}$, to be in (-0.4, 0.4). Hence, with this limitation, all possible phase shift ratios will be in the nearly linear operating region. Besides, it is worth to notice that power of load ports is larger than or equal to zero because of the resistive load. Therefore, based on (2.3), it exists

$$\sum_{m=1,m\neq j}^{n} d_{j,m}\left(1-\left|d_{j,m}\right|\right) \geq 0 \quad (j=2,3,\dots,n) \tag{4.1}$$

$$\hat{I}_j = \sum_{m=1,m\neq j}^{n}\left[\frac{1}{2N_{j,m}f_sL_{j,m}}(d_{j,1}-d_{m,1})\left(1-\left|d_{j,1}-d_{m,1}\right|\right)\hat{V}_m + \frac{V_m}{2N_{j,m}f_sL_{j,m}}\left(-1+\left|2d_{j,1}-2d_{m,1}\right|\right)\hat{d}_{m,1} + \frac{V_m}{2N_{j,m}f_sL_{j,m}}\left(1-\left|2d_{j,1}-2d_{m,1}\right|\right)\hat{d}_{j,1}\right]$$
$$(j = 1, 2, \dots, n) \tag{3.2}$$

TABLE I
THE SMALL SIGNAL GAINS

Small signals to $\hat{\boldsymbol{I}}_j$	Gain	Expression	Condition $(m, j \in N^*)$
$\hat{\boldsymbol{V}}_m$	G_{2m-3}	$\frac{1}{2N_{1,m}f_sL_{1,m}}d_{1,m}\left(1-\left\|d_{1,m}\right\|\right)T_D$	$j=1$ $2\le m\le n$
	$G_{2m+(j-1)(2n-2)-1}$	$\frac{1}{2N_{j,m}f_sL_{j,m}}(d_{j,1}-d_{m,1})\left(1-\left\|d_{j,1}-d_{m,1}\right\|\right)T_D$	$2\le j\le n$ $2\le m\le j-1$
	$G_{2m+(j-1)(2n-2)-3}$	$\frac{1}{2N_{j,m}f_sL_{j,m}}(d_{j,1}-d_{m,1})\left(1-\left\|d_{j,1}-d_{m,1}\right\|\right)T_D$	$2\le j\le n$ $j+1\le m\le n$
$\hat{\boldsymbol{d}}_{m,1}$	G_{2m-2}	$\frac{V_m}{2N_{1,m}f_sL_{1,m}}\left(-1+\left\|2d_{1,m}\right\|\right)T_D$	$j=1$ $2\le m\le n$
	$G_{2m+(j-1)(2n-2)}$	$\frac{V_m}{2N_{j,m}f_sL_{j,m}}\left(-1+\left\|2d_{j,1}-2d_{m,1}\right\|\right)T_D$	$2\le j\le n$ $2\le m\le j-1$
	$G_{2m+(j-1)(2n-2)-2}$	$\frac{V_m}{2N_{j,m}f_sL_{j,m}}\left(-1+\left\|2d_{j,1}-2d_{m,1}\right\|\right)T_D$	$2\le j\le n$ $j+1\le m\le n$
$\hat{\boldsymbol{V}}_1$	$G_{(j-1)(2n-2)+1}$	$\frac{1}{2N_{j,1}f_sL_{j,1}}d_{j,1}\left(1-\left\|d_{j,1}\right\|\right)T_D$	$2\le j\le n$
$\hat{\boldsymbol{d}}_{j,1}$	$G_{(j-1)(2n-2)+2}$	$\frac{V_1}{2N_{j,1}f_sL_{j,1}}\left(1-\left\|2d_{j,1}\right\|\right)T_D+\sum_{m=2(m\neq j)}^{n}\frac{V_m}{2N_{j,m}f_sL_{j,m}}\left(1-\left\|2d_{j,1}-2d_{m,1}\right\|\right)T_D$	$2\le j\le n$

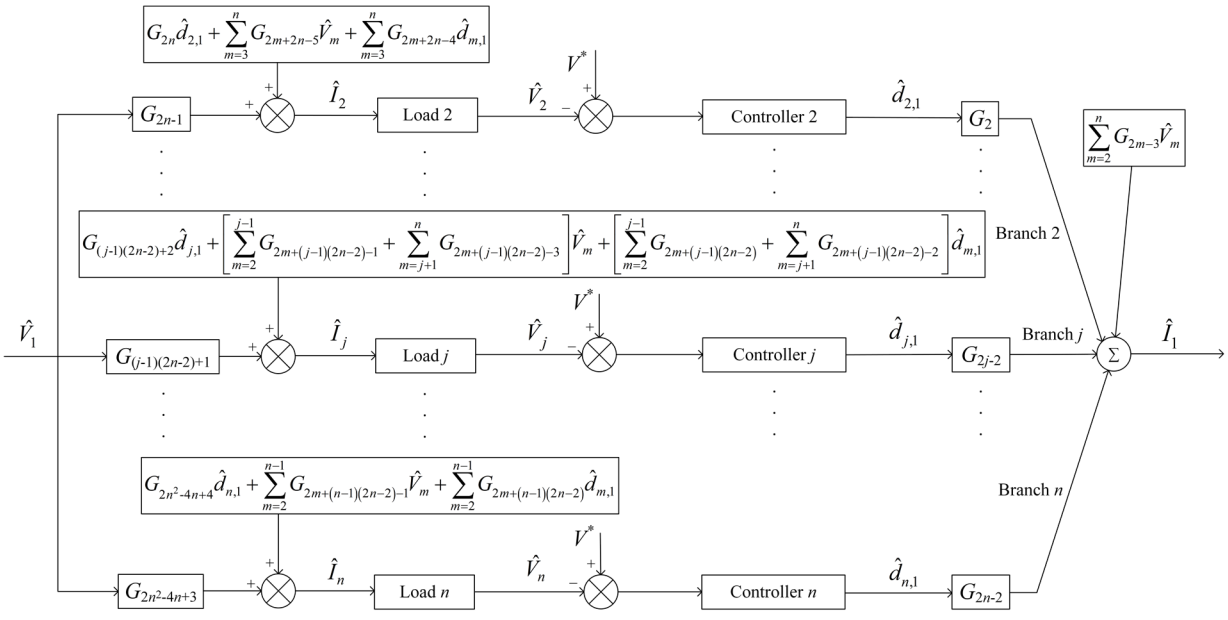

Fig. 5. The transfer function block scheme of MAB converter

$$\{\hat{V}_1\} = \begin{Bmatrix} \frac{G_{2n}G_{\mathrm{Ctrl},2}G_{\mathrm{Load},2}+1}{-G_2G_{\mathrm{Ctrl},2}G_{\mathrm{Load},2}G_{2n-1}} & \frac{G_{\mathrm{Ctrl},3}G_{2n+2}-G_{2n+1}}{-G_4G_{\mathrm{Ctrl},3}G_{2n-1}} & \cdots & \frac{G_{\mathrm{Ctrl},n}G_{4n-4}-G_{4n-5}}{-G_{2n-2}G_{\mathrm{Ctrl},n}G_{2n-1}} \\ \frac{G_{\mathrm{Ctrl},2}G_{4n}-G_{4n-1}}{-G_2G_{\mathrm{Ctrl},2}G_{4n-3}} & \frac{G_{4n-2}G_{\mathrm{Ctrl},3}G_{\mathrm{Load},3}+1}{-G_4G_{\mathrm{Ctrl},3}G_{\mathrm{Load},3}G_{4n-3}} & \cdots & \frac{G_{\mathrm{Ctrl},n}G_{6n-6}-G_{6n-7}}{-G_{2n-2}G_{\mathrm{Ctrl},n}G_{4n-3}} \\ \vdots & \vdots & \vdots & \vdots \\ \frac{G_{\mathrm{Ctrl},2}G_{(n-1)(2n-2)+4}-G_{(n-1)(2n-2)+3}}{-G_2G_{\mathrm{Ctrl},2}G_{(n-1)(2n-2)+1}} & \frac{G_{\mathrm{Ctrl},3}G_{(n-1)(2n-2)+6}-G_{(n-1)(2n-2)+5}}{-G_4G_{\mathrm{Ctrl},3}G_{(n-1)(2n-2)+1}} & \cdots & \frac{G_{(n-1)(2n-2)+2}G_{\mathrm{Ctrl},n}G_{\mathrm{Load},n}+1}{-G_{2n-2}G_{\mathrm{Ctrl},n}G_{\mathrm{Load},n}G_{(n-1)(2n-2)+1}} \end{Bmatrix} \begin{Bmatrix} G_{\mathrm{Branch},2} \\ G_{\mathrm{Branch},3} \\ \vdots \\ G_{\mathrm{Branch},n} \end{Bmatrix} = \boldsymbol{A}\{\boldsymbol{B}\}$$
(3.5)

Row: $j = 2,3,\dots n$

Column: $m = 2,3,\dots n$

V. Input Impedance Validation of MAB Converter

In this section, the TAB converter and the QAB converter are chosen to be validated with the generalized model, while Matlab is used to plot the input impedance of converter and an ideal switching model is built in PLECS to measure and verify the input impedance. A preliminary validation for the input impedance of TAB converter has been already done and shown in [24].

A. Simulation verification of TAB converter

Considering the TAB converter has three ports, totally twelve small signal gains can be obtained for transfer function block scheme. The gains are given as Table III in Appendix. According to (3.5), Matrix $\boldsymbol{A}$ can be written as

$$\boldsymbol{A}=\begin{Bmatrix} \frac{G_6G_{\mathrm{Ctrl},2}G_{\mathrm{Load},2}+1}{-G_2G_{\mathrm{Ctrl},2}G_{\mathrm{Load},2}G_5} & \frac{G_{\mathrm{Ctrl},3}G_8-G_7}{-G_4G_{\mathrm{Ctrl},3}G_5} \\ \frac{G_{\mathrm{Ctrl},2}G_{12}-G_{11}}{-G_2G_{\mathrm{Ctrl},2}G_9} & \frac{G_{10}G_{\mathrm{Ctrl},3}G_{\mathrm{Load},3}+1}{-G_4G_{\mathrm{Ctrl},3}G_{\mathrm{Load},3}G_9} \end{Bmatrix} \quad (5.1)$$

With the known Matrix $\boldsymbol{A}$ in (5.1), the input impedance of TAB converter can be obtained following the equations from (3.6) to (3.9) in Section III. Fig. 6 shows the bode plot of input impedance of TAB converter. It can be observed that the input impedance of TAB converter behaves as a CPL at low frequencies and behaves as a capacitor at high frequencies in both symmetrical (i.e. same load power) and asymmetrical (i.e. different load power) power flow modes. Furthermore, the input power influences the input impedance at low frequencies because of the negative incremental impedance characteristic. The lower the input power, the higher the input impedance and vice versa.

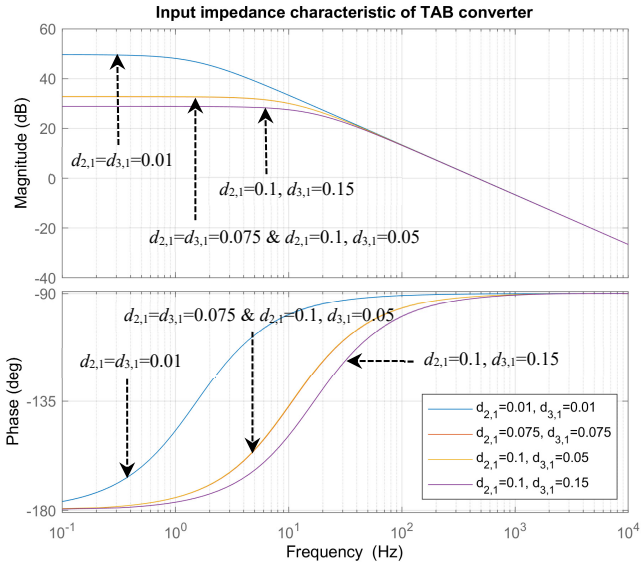

Fig. 6. Input impedance characteristic of TAB converter

To verify the input impedance of TAB converter, a switching model is created in PLECS. The methodology is injecting sinusoidal AC current with different frequencies into input current while observing the variations in input voltage. In the following verification, two cases in Fig. 6 are chosen in which power flows symmetrically and asymmetrically: Case 1: $d_{2,1} = d_{3,1} = 0.075$ and Case 2: $d_{2,1} = 0.1$, $d_{3,1} = 0.15$. The simulation measurements are plotted with the bode diagram to make a comparison. The comparison results are shown in Fig. 7 and Fig. 8.

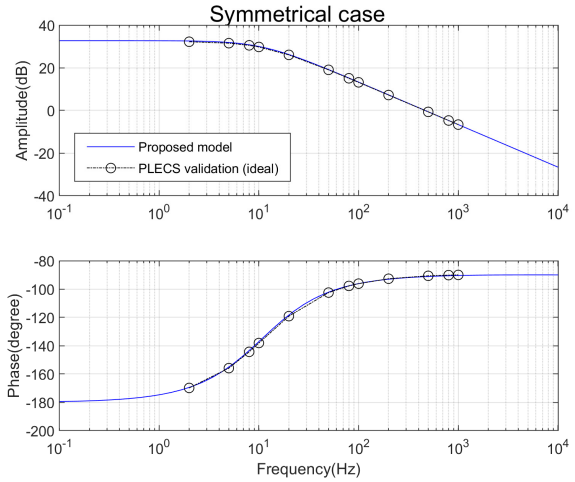

Fig. 7. Case 1: $d_{2,1} = d_{3,1} = 0.075$, symmetrical power flow

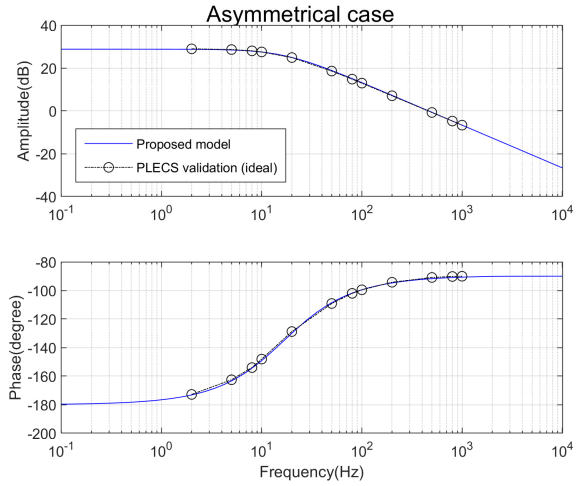

Fig. 8. Case 2: $d_{2,1} = 0.1$, $d_{3,1} = 0.15$, asymmetrical power flow

As Fig. 7 and Fig. 8 shows, the simulation measurements are consistent with the bode plot. This proves that the input impedance model is correct for both symmetrical and asymmetrical power flow modes.

B. Simulation verification of QAB converter

Since the QAB converter has four ports, there are totally twenty four gains. They are given as Table IV in Appendix. According to (3.5), Matrix $\boldsymbol{A}$ can be written as

$$\boldsymbol{A}=\begin{Bmatrix} \frac{G_8G_{\mathrm{Ctrl},2}G_{\mathrm{Load},2}+1}{-G_2G_{\mathrm{Ctrl},2}G_{\mathrm{Load},2}G_7} & \frac{G_{\mathrm{Ctrl},3}G_{10}-G_9}{-G_4G_{\mathrm{Ctrl},3}G_7} & \frac{G_{\mathrm{Ctrl},4}G_{12}-G_{11}}{-G_6G_{\mathrm{Ctrl},4}G_7} \\ \frac{G_{\mathrm{Ctrl},2}G_{16}-G_{15}}{-G_2G_{\mathrm{Ctrl},2}G_{13}} & \frac{G_{14}G_{\mathrm{Ctrl},3}G_{\mathrm{Load},3}+1}{-G_4G_{\mathrm{Ctrl},3}G_{\mathrm{Load},3}G_{13}} & \frac{G_{\mathrm{Ctrl},4}G_{18}-G_{17}}{-G_6G_{\mathrm{Ctrl},4}G_{13}} \\ \frac{G_{\mathrm{Ctrl},2}G_{22}-G_{21}}{-G_2G_{\mathrm{Ctrl},2}G_{19}} & \frac{G_{\mathrm{Ctrl},3}G_{24}-G_{23}}{-G_4G_{\mathrm{Ctrl},3}G_{19}} & \frac{G_{20}G_{\mathrm{Ctrl},4}G_{\mathrm{Load},4}+1}{-G_6G_{\mathrm{Ctrl},4}G_{\mathrm{Load},4}G_{19}} \end{Bmatrix} \quad (5.2)$$

Again, following the equations from (3.6) to (3.9) in Section III, the input impedance bode diagram of QAB converter is worked out and shown in Fig. 9, which is similar to Fig. 6. The input impedance of QAB converter also behaves as a CPL at low frequencies and behaves as a capacitor at high frequencies. In addition, the input power influences the input impedance at

low frequencies. The higher the input power, the lower the input impedance and vice versa. To verify the input impedance of QAB converter, the methodology is same as verification approach for TAB converter. Two cases in Fig. 9 are chosen in which power flows symmetrically and asymmetrically: Case 1: $d_{2,1}$=$d_{3,1}$=$d_{4,1}$=0.1 and Case 2: $d_{2,1}$=$d_{3,1}$=0.05, $d_{4,1}$=0.08. The simulation measurements are plotted with the bode diagram to make a comparison, shown in Fig. 10 and Fig. 11. It is obvious that the simulation measurements are consistent with the bode plot, proving the validity of proposed input impedance model in QAB converter as well.

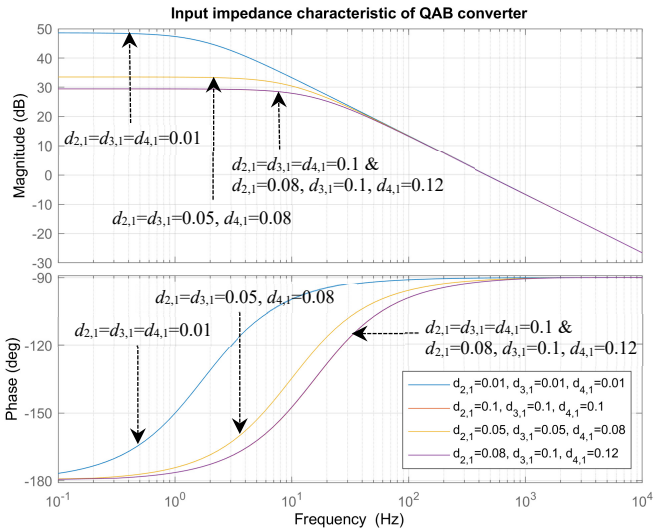

Fig. 9. Input impedance characteristic of QAB converter

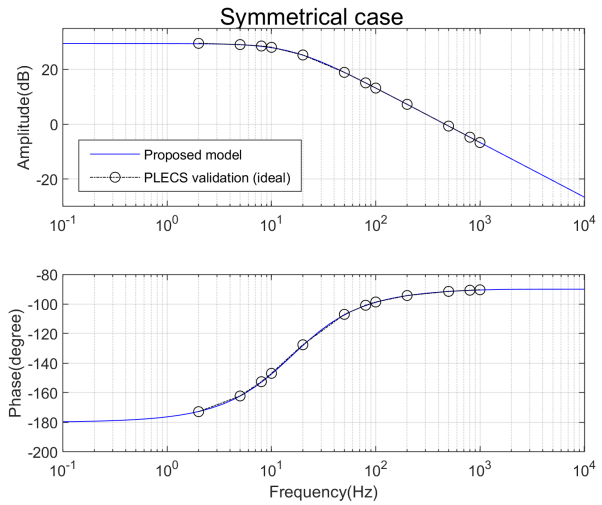

Fig. 10. Case 1: $d_{2,1}$=$d_{3,1}$=$d_{4,1}$=0.1, symmetrical power flow

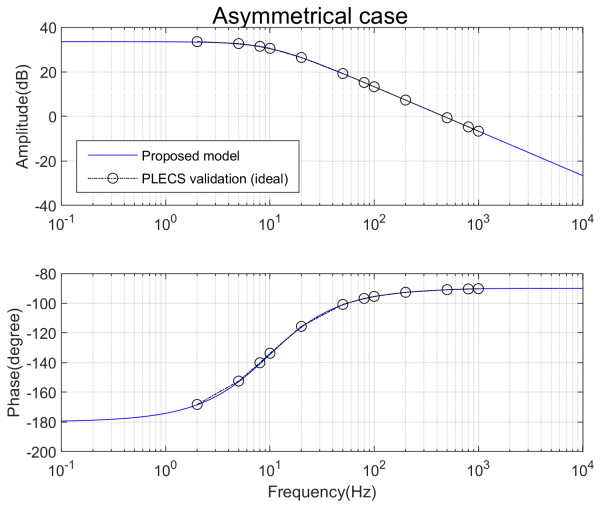

Fig. 11. Case 2: $d_{2,1}$=$d_{3,1}$=0.05, $d_{4,1}$=0.08, asymmetrical power flow

VI. Experimental Results

In this section, the experimental setup and experimental results are given. As for experimental setup, a QAB converter experimental prototype with symmetrical structure is built and shown in Fig. 12. The experimental setup of TAB converter can be realized by disconnecting an H-Bridge from the transformer. As for experimental results, the input impedance of TAB converter and QAB converter is measured and compared to the proposed input impedance model, and to the PLECS switching model in which the value of magnetizing inductance and winding resistance of transformer, on-state resistance of MOSFET and dead time of switching are added in accordance with the experimental setup.

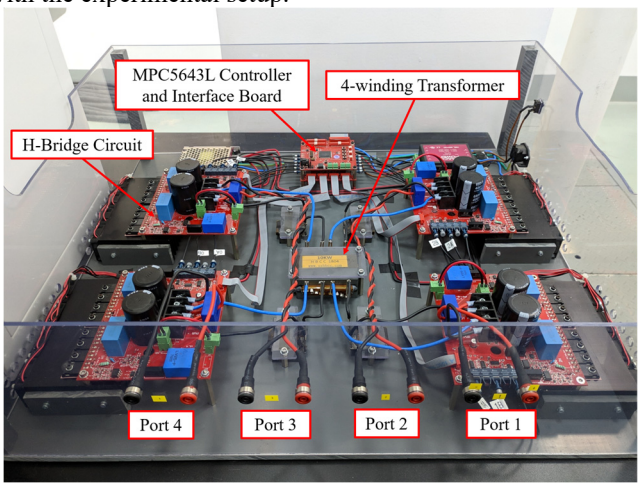

Fig. 12. Experimental prototype

Considering the specifications of the experimental setup, a different set of parameters is chosen for the experimental verification, also, the non-ideal characteristics which were not considered before, are measured from this setup directly. They are listed in Table V. During the experiments, both symmetrical power flow case and asymmetrical power flow case of TAB converter and QAB converter are carried out.

TABLE V
THE MODIFIED PARAMETERS FOR EXPERIMENTS

Symbol	Definition	Value
V_1, V_2…V_n	Port voltage	50 V
f_s	Switching frequency	10 kHz
K_{p2}, K_{p3}…K_{pn}	Proportional coefficient	0.02
K_{i2}, K_{i3}…K_{in}	Integral coefficient	1
L_m	Magnetizing inductance	3 mH
R_w	Winding resistance	0.2 ohm
R_{on}	On-state resistance of MOSFET	0.025 ohm
T_{dead}	Dead time of switching	1 μs

A. Experimental verification of TAB converter

To measure the input impedance of TAB converter, Port 1 is connected to power supply, Port 2 and Port 3 are connected to loads, and the H-Bridge of Port 4 is disconnected from the

transformer.

1) Symmetrical power flow case

In symmetrical power flow case of TAB converter, Port 2 and Port 3 are connected to the same 8.3 ohm resistive load. The simulation results and experimental results are shown in Fig. 13.

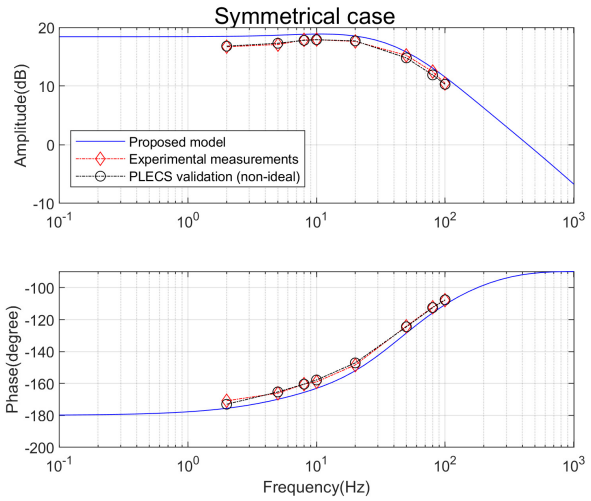

Fig. 13. Simulation and experimental measurements of TAB converter in symmetrical power flow case

2) Asymmetrical power flow case

In asymmetrical power flow case of TAB converter, Port 2 is connected to a 16.7 ohm resistive load and Port 3 is connected to a 10 ohm resistive load. The simulation results and experimental results are shown in Fig. 14.

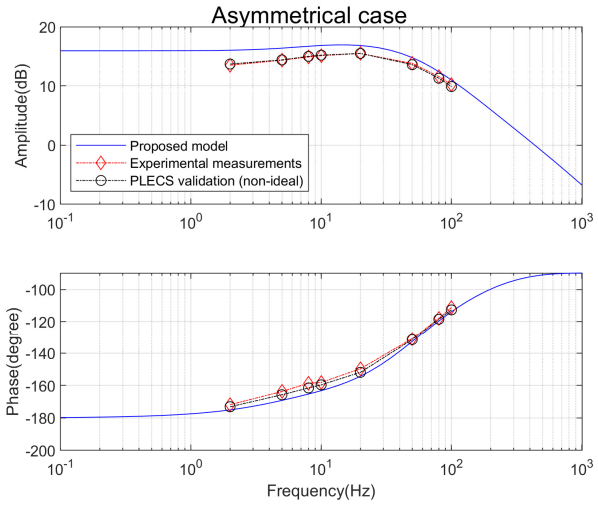

Fig. 14. Simulation and experimental measurements of TAB converter in asymmetrical power flow case

B. Experimental verification of QAB converter

As for the input impedance measurements of QAB converter, Port 1 is connected to the power supply, Port 2, Port 3 and Port 4 is connected to resistive loads.

1) Symmetrical power flow case

In symmetrical power flow case of QAB converter, Port 2, Port 3 and Port 4 are connected to the same 8.3 ohm resistive load. The simulation results and experimental results are shown in Fig. 15.

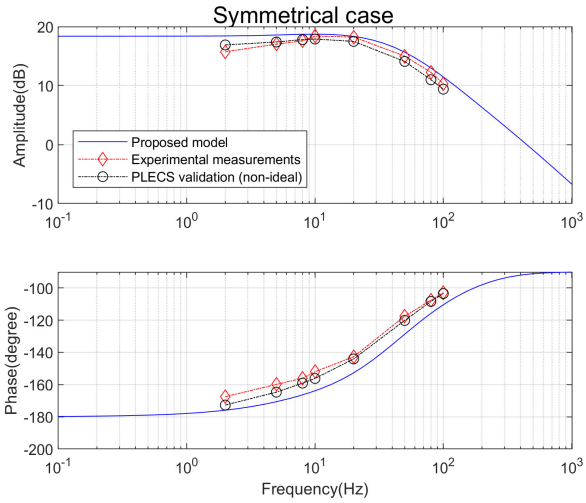

Fig. 15. Simulation and experimental measurements of QAB converter in symmetrical power flow case

2) Asymmetrical power flow case

In asymmetrical power flow case of QAB converter, Port 2 is connected to a 16.7 ohm resistive load, Port 3 and Port 4 are connected to another 16.7 ohm resistive load together. The simulation results and experimental results are shown in Fig. 16.

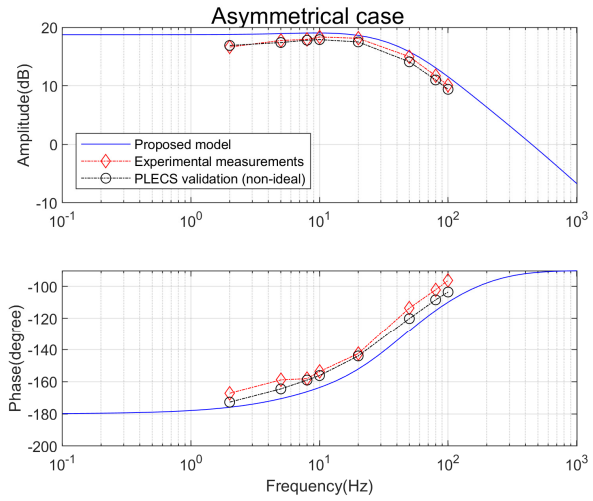

Fig. 16. Simulation and experimental measurements of QAB converter in asymmetrical power flow case

As Fig. 13 to Fig. 16 shows, the experimental measurements are consistent with the proposed model. This also proves the validity of the proposed model in assessing the stability of systems containing MAB converters. In addition, with the aid of PLECS switching model, it is noted that the mismatch between the proposed model and measurements can be caused by the non-ideal characteristics of the converter. These non-ideal characteristics can be regarded as damping, making the input impedance more resistive. As a result, the amplitude of input impedance is a bit lower and the phase is a bit higher in reality.

VII. Conclusion

This paper has thoroughly investigated the impedance modeling for multi-port power converters in symmetrical and asymmetrical power transfer condition. The theoretical model is validated against switching simulations and experimental results, showing a good matching. It can be concluded that the proposed model can be used to represent the multi-port system in near actual condition. The multi-port converter exhibits a constant power load behavior at lower frequencies, whereas at higher frequencies the input capacitor dominates the input impedance. Once the input impedance is known, further stability studies based on the impedance criterion can be carried out to evaluate the system behavior in a complex network configuration. These results can be also used for system design and optimization, allowing to find the minimum input capacitance value that guarantees the system stability.

Appendix

The small signal gains of TAB converter are given as Table III below:

TABLE III
THE GAINS OF TAB CONVERTER

Gain	Expression
G_1	$\frac{1}{2N_{1,2}f_sL_{1,2}}d_{1,2}(1-\lvert d_{1,2}\rvert)T_D$
G_2	$\frac{V_2}{2N_{1,2}f_sL_{1,2}}(-1+\lvert 2d_{1,2}\rvert)T_D$
G_3	$\frac{1}{2N_{1,3}f_sL_{1,3}}d_{1,3}(1-\lvert d_{1,3}\rvert)T_D$
G_4	$\frac{V_3}{2N_{1,3}f_sL_{1,3}}(-1+\lvert 2d_{1,3}\rvert)T_D$
G_5	$\frac{1}{2N_{2,1}f_sL_{2,1}}d_{2,1}(1-\lvert d_{2,1}\rvert)T_D$
G_6	$\frac{V_1}{2N_{2,1}f_sL_{2,1}}(1-\lvert 2d_{2,1}\rvert)T_D+\frac{V_3}{2N_{2,3}f_sL_{2,3}}(1-\lvert 2d_{2,1}-2d_{3,1}\rvert)T_D$
G_7	$\frac{1}{2N_{2,3}f_sL_{2,3}}(d_{2,1}-d_{3,1})(1-\lvert d_{2,1}-d_{3,1}\rvert)T_D$
G_8	$\frac{V_3}{2N_{2,3}f_sL_{2,3}}(-1+\lvert 2d_{2,1}-2d_{3,1}\rvert)T_D$
G_9	$\frac{1}{2N_{3,1}f_sL_{3,1}}d_{3,1}(1-\lvert d_{3,1}\rvert)T_D$
G_{10}	$\frac{V_1}{2N_{3,1}f_sL_{3,1}}(1-\lvert 2d_{3,1}\rvert)T_D+\frac{V_2}{2N_{3,2}f_sL_{3,2}}(1-\lvert 2d_{3,1}-2d_{2,1}\rvert)T_D$
G_{11}	$\frac{1}{2N_{3,2}f_sL_{3,2}}(d_{3,1}-d_{2,1})(1-\lvert d_{3,1}-d_{2,1}\rvert)T_D$
G_{12}	$\frac{V_2}{2N_{3,2}f_sL_{3,2}}(-1+\lvert 2d_{3,1}-2d_{2,1}\rvert)T_D$

The small signal gains of QAB converter are given as Table IV below:

TABLE IV
THE GAINS OF QAB CONVERTER

Gain	Expression
G_1	$\frac{1}{2N_{1,2}f_sL_{1,2}}d_{1,2}(1-\lvert d_{1,2}\rvert)T_D$
G_2	$\frac{V_2}{2N_{1,2}f_sL_{1,2}}(-1+\lvert 2d_{1,2}\rvert)T_D$
G_3	$\frac{1}{2N_{1,3}f_sL_{1,3}}d_{1,3}(1-\lvert d_{1,3}\rvert)T_D$
G_4	$\frac{V_3}{2N_{1,3}f_sL_{1,3}}(-1+\lvert 2d_{1,3}\rvert)T_D$
G_5	$\frac{1}{2N_{1,4}f_sL_{1,4}}d_{1,4}(1-\lvert d_{1,4}\rvert)T_D$
G_6	$\frac{V_4}{2N_{1,4}f_sL_{1,4}}(-1+\lvert 2d_{1,4}\rvert)T_D$
G_7	$\frac{1}{2N_{2,1}f_sL_{2,1}}d_{2,1}(1-\lvert d_{2,1}\rvert)T_D$
G_8	$\frac{V_1}{2N_{2,1}f_sL_{2,1}}(1-\lvert 2d_{2,1}\rvert)T_D+\frac{V_3}{2N_{2,3}f_sL_{2,3}}(1-\lvert 2d_{2,1}-2d_{3,1}\rvert)T_D+\frac{V_4}{2N_{2,4}f_sL_{2,4}}(1-\lvert 2d_{2,1}-2d_{4,1}\rvert)T_D$
G_9	$\frac{1}{2N_{2,3}f_sL_{2,3}}(d_{2,1}-d_{3,1})(1-\lvert d_{2,1}-d_{3,1}\rvert)T_D$
G_{10}	$\frac{V_3}{2N_{2,3}f_sL_{2,3}}(-1+\lvert 2d_{2,1}-2d_{3,1}\rvert)T_D$
G_{11}	$\frac{1}{2N_{2,4}f_sL_{2,4}}(d_{2,1}-d_{4,1})(1-\lvert d_{2,1}-d_{4,1}\rvert)T_D$
G_{12}	$\frac{V_4}{2N_{2,4}f_sL_{2,4}}(-1+\lvert 2d_{2,1}-2d_{4,1}\rvert)T_D$
G_{13}	$\frac{1}{2N_{3,1}f_sL_{3,1}}d_{3,1}(1-\lvert d_{3,1}\rvert)T_D$
G_{14}	$\frac{V_1}{2N_{3,1}f_sL_{3,1}}(1-\lvert 2d_{3,1}\rvert)T_D+\frac{V_2}{2N_{3,2}f_sL_{3,2}}(1-\lvert 2d_{3,1}-2d_{2,1}\rvert)T_D+\frac{V_4}{2N_{3,4}f_sL_{3,4}}(1-\lvert 2d_{3,1}-2d_{4,1}\rvert)T_D$
G_{15}	$\frac{1}{2N_{3,2}f_sL_{3,2}}(d_{3,1}-d_{2,1})(1-\lvert d_{3,1}-d_{2,1}\rvert)T_D$
G_{16}	$\frac{V_2}{2N_{3,2}f_sL_{3,2}}(-1+\lvert 2d_{3,1}-2d_{2,1}\rvert)T_D$
G_{17}	$\frac{1}{2N_{3,4}f_sL_{3,4}}(d_{3,1}-d_{4,1})(1-\lvert d_{3,1}-d_{4,1}\rvert)T_D$
G_{18}	$\frac{V_4}{2N_{3,4}f_sL_{3,4}}(-1+\lvert 2d_{3,1}-2d_{4,1}\rvert)T_D$
G_{19}	$\frac{1}{2N_{4,1}f_sL_{4,1}}d_{4,1}(1-\lvert d_{4,1}\rvert)T_D$
G_{20}	$\frac{V_1}{2N_{4,1}f_sL_{4,1}}(1-\lvert 2d_{4,1}\rvert)T_D+\frac{V_2}{2N_{4,2}f_sL_{4,2}}(1-\lvert 2d_{4,1}-2d_{2,1}\rvert)T_D+\frac{V_3}{2N_{4,3}f_sL_{4,3}}(1-\lvert 2d_{4,1}-2d_{3,1}\rvert)T_D$
G_{21}	$\frac{1}{2N_{4,2}f_sL_{4,2}}(d_{4,1}-d_{2,1})(1-\lvert d_{4,1}-d_{2,1}\rvert)T_D$
G_{22}	$\frac{V_2}{2N_{4,2}f_sL_{4,2}}(-1+\lvert 2d_{4,1}-2d_{2,1}\rvert)T_D$
G_{23}	$\frac{1}{2N_{4,3}f_sL_{4,3}}(d_{4,1}-d_{3,1})(1-\lvert d_{4,1}-d_{3,1}\rvert)T_D$
G_{24}	$\frac{V_3}{2N_{4,3}f_sL_{4,3}}(-1+\lvert 2d_{4,1}-2d_{3,1}\rvert)T_D$

REFERENCES

[1] S. J. Cutts, "A collaborative approach to the More Electric Aircraft," in *2002 International Conference on Power Electronics, Machines and Drives (Conf. Publ. No. 487)*, 2002, pp. 223–228.

[2] J. S. Cloyd, "Status of the United States Air Force's More Electric Aircraft initiative," *IEEE Aerospace and Electronic Systems Magazine*, vol. 13, no. 4, pp. 17–22, Apr. 1998.

[3] J. A. Rosero, J. A. Ortega, E. Aldabas, and L. Romeral, "Moving towards a more electric aircraft," *IEEE Aerospace and Electronic Systems Magazine*, vol. 22, no. 3, pp. 3–9, Mar. 2007.

[4] B. Sarlioglu and C. T. Morris, "More Electric Aircraft: Review, Challenges, and Opportunities for Commercial Transport Aircraft," *IEEE Transactions on Transportation Electrification*, vol. 1, no. 1, pp. 54–64, Jun. 2015.

[5] G. Buticchi, S. Bozhko, M. Liserre, P. Wheeler, and K. Al-Haddad, "On-Board Microgrids for the More Electric Aircraft—Technology Review," *IEEE Transactions on Industrial Electronics*, vol. 66, no. 7, pp. 5588–5599, Jul. 2019.

[6] P. Wheeler and S. Bozhko, "The More Electric Aircraft: Technology and challenges.," *IEEE Electrification Magazine*, vol. 2, no. 4, pp. 6–12, Dec. 2014.

[7] G. Buticchi, L. Costa, and M. Liserre, "Improving System Efficiency for the More Electric Aircraft: A Look at dc\/dc Converters for the Avionic Onboard dc Microgrid," *IEEE Industrial Electronics Magazine*, vol. 11, no. 3, pp. 26–36, Sep. 2017.

[8] D. Salomonsson and A. Sannino, "Low-Voltage DC Distribution System for Commercial Power Systems With Sensitive Electronic Loads," *IEEE Transactions on Power Delivery*, vol. 22, no. 3, pp. 1620–1627, Jul. 2007.

[9] H. Tao, A. Kotsopoulos, J. L. Duarte, and M. A. M. Hendrix, "Family of multiport bidirectional DC-DC converters," *IEE Proceedings - Electric Power Applications*, vol. 153, no. 3, pp. 451–458, May 2006.

[10] M. N. Kheraluwala, R. W. Gascoigne, D. M. Divan, and E. D. Baumann, "Performance characterization of a high-power dual active bridge DC-to-DC converter," *IEEE Transactions on Industry Applications*, vol. 28, no. 6, pp. 1294–1301, Nov. 1992.

[11] C. Zhao, S. D. Round, and J. W. Kolar, "An Isolated Three-Port Bidirectional DC-DC Converter With Decoupled Power Flow Management," *IEEE Transactions on Power Electronics*, vol. 23, no. 5, pp. 2443–2453, Sep. 2008.

[12] G. Buticchi, L. F. Costa, D. Barater, M. Liserre, and E. D. Amarillo, "A Quadruple Active Bridge Converter for the Storage Integration on the More Electric Aircraft," *IEEE Transactions on Power Electronics*, vol. 33, no. 9, pp. 8174–8186, Sep. 2018.

[13] H. Tao, H. Hu, X. Wang, F. Blaabjerg, and Z. He, "Impedance-Based Harmonic Instability Assessment in a Multiple Electric Trains and Traction Network Interaction System," *IEEE Transactions on Industry Applications*, vol. 54, no. 5, pp. 5083–5096, Sep. 2018.

[14] A. Riccobono and E. Santi, "Comprehensive Review of Stability Criteria for DC Power Distribution Systems," *IEEE Transactions on Industry Applications*, vol. 50, no. 5, pp. 3525–3535, Sep. 2014.

[15] R. D. Middlebrook, "Input filter considerations in design and application of switching regulators," in *Conf. Rec. IEEE IAS Annu. Meeting*, 1976, pp. 366–382.

[16] X. Feng, J. Liu, and F. C. Lee, "Impedance specifications for stable DC distributed power systems," *IEEE Transactions on Power Electronics*, vol. 17, no. 2, pp. 157–162, Mar. 2002.

[17] C. M. Wildrick, F. C. Lee, B. H. Cho, and B. Choi, "A method of defining the load impedance specification for a stable distributed power system," *IEEE Transactions on Power Electronics*, vol. 10, no. 3, pp. 280–285, May 1995.

[18] D. Lu, X. Wang, and F. Blaabjerg, "Impedance-Based Analysis of DC-Link Voltage Dynamics in Voltage-Source Converters," *IEEE Transactions on Power Electronics*, vol. 34, no. 4, pp. 3973–3985, Apr. 2019.

[19] F. Gao, S. Bozhko, A. Costabeber, G. Asher, and P. Wheeler, "Control Design and Voltage Stability Analysis of a Droop-Controlled Electrical Power System for More Electric Aircraft," *IEEE Transactions on Industrial Electronics*, vol. 64, no. 12, pp. 9271–9281, Dec. 2017.

[20] J. L. Duarte, M. Hendrix, and M. G. Simoes, "Three-Port Bidirectional Converter for Hybrid Fuel Cell Systems," *IEEE Transactions on Power Electronics*, vol. 22, no. 2, pp. 480–487, Mar. 2007.

[21] R. W. Erikson and D. Maksimovic, Fundamentals of power electronics, 2nd ed. Norwell, Mass.: Kluwer Academic, 2001.

[22] H. Qin and J. W. Kimball, "Generalized Average Modeling of Dual Active Bridge DC–DC Converter," *IEEE Transactions on Power Electronics*, vol. 27, no. 4, pp. 2078–2084, Apr. 2012.

[23] M. Khazraei, V. A. K. Prabhala, R. Ahmadi, and M. Ferdowsi, "Solid-state transformer stability and control considerations," in *2014 IEEE Applied Power Electronics Conference and Exposition - APEC 2014*, 2014, pp. 2237–2244.

[24] J. Yang, G. Buticchi, C. Gu, S. Günter, H. Yan, and P. Wheeler, "Transfer Function Based Input Impedance Determination of Triple Active Bridge Converter," in *IECON 2019 - 45th Annual Conference of the IEEE Industrial Electronics Society*, 2019, vol. 1, pp. 4917–4923.

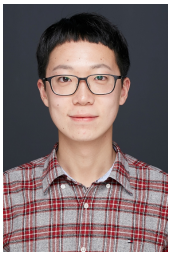

Jiajun Yang (S'18) received the B.Eng. degree (Hons.) in electrical and electronic engineering in 2017, from the University of Nottingham Ningbo China, Ningbo, China, where he is currently working toward the Ph.D. degree with the Key Laboratory of More Electric Aircraft Technology of Zhejiang Province.

From 2017 to 2018, he was a hardware engineer with the Nottingham Electrification Centre. His current research interests include high power density dc-dc converters and stability analysis of dc microgrids for the more electric aircraft.

Giampaolo Buticchi (S'10-M'13-SM'17) received the Master degree in Electronic Engineering in 2009 and the Ph.D degree in Information Technologies in 2013 from the University of Parma, Italy. In 2012 he was visiting researcher at The University of Nottingham, UK. Between 2014 and 2017, he was a post-doctoral researcher and Von Humboldt Post-doctoral Fellow at the University of Kiel, Germany.

He is now Associate Professor in Electrical Engineering at The University of Nottingham Ningbo China and the Head of Power Electronics of the Nottingham Electrification Center. His research focuses on power electronics for renewable energy systems, smart transformer fed micro-grids and dc grids for the More Electric Aircraft. He is author/co-author of more than 200 scientific papers and an Associate Editor of the IEEE Transactions on Industrial Electronics and of the IEEE Transactions on Transportation Electrification.

He is the Chair of the IEEE Industrial Electronics Society Technical Committee on Renewable Energy Systems.

Chunyang Gu (S'12–M'15) was born in Heilongjiang, China, in 1988. She received BSc degree from Harbin Institute of Technology, Harbin, China, in 2010, and PhD degree from Tsinghua University, Beijing, China, in 2015, both in electrical engineering. In 2015, she went to the University of Nottingham, UK, where she was a postdoc research fellow in Power Electronics, Machines and Control (PEMC) Research Group.

Since 2017, she has been an Assistant Professor in Department of Electrical and Electronic Engineering and PEMC Research Group, University of Nottingham Ningbo China. Her research interests include power electronics for transportation electrification, renewable energy and grid applications, e.g. solid-state transformer, solid-state circuit breaker, multi-level converter topologies and control, application of wide-band-gap semiconductor devices, power electronics in EV, railway, marine and MEA.

Sandro Günter (S'14-M'18) received the M.Sc. degree in Electrical Engineering from the University of Duisburg-Essen, Germany in 2011. From 2012 to 2017, he worked as a post graduate researcher at the Chair of Power Electronics of the University of Kiel, Germany where he received the Ph.D. degree in 2017. Between 2017 and 2018 he was a postdoctoral researcher at the University of Nottingham Ningbo, China. He is currently a R&D Engineer at E3/DC GmbH in Germany. His research interests include grid connected multilevel converters as well as isolated DC/DC converters.

He Zhang (M'14-SM'18) received his B.Eng. degree in Control Science and Engineering from Zhejiang University, China, in 2002. He obtained the MSc. and Ph.D. degree in electrical machines from The University of Nottingham, UK, in 2004 and 2009 respectively. After this he worked as Research Fellow at the University and Director of BestMotion Technology Centre. He moved to University of Nottingham Ningbo China as Senior Research Fellow in 2014 and Principal Research Fellow in 2016. Currently he is the Director of Nottingham Electrification Centre (NEC) within the Power electronics, Machines and Control research group in University Of Nottingham. His research interests include high performance electric machines and drives for transport electrification.

Pat Wheeler (M'99–SM'11) received his BEng [Hons] degree in 1990 from the University of Bristol, UK. He received his PhD degree in Electrical Engineering for his work on Matrix Converters from the University of Bristol, UK in 1994. In 1993 he moved to the University of Nottingham and worked as a research assistant in the Department of Electrical and Electronic Engineering. In 1996 he became a Lecturer in the Power Electronics, Machines and Control Group at the University of Nottingham, UK. Since January 2008 he has been a Full Professor in the same research group. He was Head of the Department of Electrical and Electronic Engineering at the University of Nottingham from 2015 to 2018. He is currently the Head of the Power Electronics, Machines and Control Research Group, Global Direcotr of the University of Nottingham's Institute of Aerosapce Technology and is the Li Dak Sum Chair Professor in Electrical and Aerospace Engineering. He is a member of the IEEE PELs AdCom and was an IEEE PELs Distinguished Lecturer from 2013 to 2017. He has published 500 academic publications in leading international conferences and journals.